

The effects and behaviour of Li and Cu alloying agents in lean Al-Mg-Si alloys

Eva A. Mørtzell*¹, Calin D. Marioara², Sigmund J. Andersen², Inga G. Ringdalen², Jesper Friis², Sigurd Wenner¹, Jostein Røyset³, Oddvin Reiso³ and Randi Holmestad¹

¹Department of Physics, Norwegian University of Science and Technology (NTNU), 7491 Trondheim, Norway

²SINTEF Materials and Chemistry, N-7465 Trondheim, Norway

³Hydro Aluminum R&D Sunndal, N-6600 Sunndalsøra, Norway

*Corresponding author. E-mail address: eva.mortzell@ntnu.no

Abstract

We show how replacing a fraction of Mg with Li in a lean Al-Mg-Si alloy gives comparable strength and enhanced temperature stability. Replacing solute with smaller amounts of Cu and Li also improves thermal stability and nearly compensates the strength loss for longer ageing times. High angle annular dark field scanning transmission electron microscopy (HAADF-STEM) documented Li and Cu causing modest structural changes to the main hardening precipitate, β'' . However, density functional theory calculations verified the observation from HAADF-STEM that Li preferentially occupies Mg3 sites in the β'' structure.

Keywords: Al-Mg-Si, TEM, HAADF-STEM, DFT, Lithium, Copper

Introduction

The major alloying elements in the age hardenable aluminium 6xxx series are Mg and Si, in typical amounts of 1 - 2 at %. Alloys of this series are rolled or extruded into final shapes. Hardening occurs during a subsequent 'artificial' ageing (AA) step – a heat treatment performed at a temperature around 180 °C. The precipitation sequence in ternary Al-Mg-Si alloys is as follows [1].

Supersaturated solid solution \rightarrow atomic clusters \rightarrow Guinier-Preston-zones (pre- β'') [2] [3] \rightarrow β'' [4] [5] \rightarrow β' [6], $U1$ [7], $U2$ [8], B' [9] \rightarrow β , Si (stable)

The majority of the hardening phases occurring at peak hardness is monoclinic β'' phase. Full coherency, small size and high number density are probably the most essential parameters behind its strengthening capabilities. In ternary alloys with Mg/Si ratios close to unity, high-resolution transmission electron microscopy (HRTEM) images taken along $\langle 001 \rangle_{Al}$ orientation reveal short needles along the two normal $\langle 100 \rangle_{Al}$ directions in the plane. The cross-sections of these β'' needles along the viewing direction appear monoclinic, with edges defined by cell parameters $a_{\beta''} \parallel \langle 3\bar{2}0 \rangle_{Al}$ and $c_{\beta''} \parallel \langle 130 \rangle_{Al}$ and the monoclinic angle 105.3°. Close-ups of the cross-section show that β'' is essentially a stack of identical units (column groups) with eye-like appearance. One 'eye' consists of nine columns with roughly 4-fold ordering (a Si_4Mg_4 ring around a central $Mg_{1-x}Al_x$ column, $0 < x < 1$) plus two less conspicuous satellite columns on

each side (ideally Aluminium), see also Fig. 5 (c, d). The satellite sites were originally assumed to be Si (Si3 positions), but later work has shown they are flexible sites, especially at the interface, where elements like Cu may be adopted to reduce strain [10]. One unit cell has two such $\text{Si}_4\text{Mg}_{4-x}\text{Al}_{2+x}$ units at the (00z) and $(\frac{1}{2}, 0, z+\frac{1}{2})$ special positions in the unit cell. They may be regarded as molecular units of β'' and were recently shown to come in three different stacking variations [11], sometimes mixed. The stacking variations occur particularly frequently with small additions of Ge, where Ge (partially) occupies some Si columns.

Increasing the amount of solute to improve strength creates a dilemma: extrudability becomes worse and less solute can lead to sacrifices in surface quality. It has been shown in previous work, that maintaining strength is possible when parts of the Mg-Si content is replaced by a lower amount of Ge [12]. The solid solubility of Li in aluminium is high. With nearly a quarter the weight of aluminium, Li also reduces alloy density somewhat [13]. Koshino et al. have shown how small additions of Li to Al-Mg-Si alloys increase the age-hardening response [14]. From the previous investigations it appears that Li can be incorporated in the precipitates, and it has been argued that it does not alter the precipitation sequence. If so, the β'' phase should still be the main hardening precipitate for these alloys, although the precipitate size, numbers and strength potential may be expected to change. Earlier studies also report how Li diffuses quickly towards the surface of the alloy and significant amounts can be depleted into air. Depletion of Li from the material surface also occurs for Al-Li alloys if the surface oxide layer has been removed [15]. It has been suggested that Li atoms diffuse to the surface faster than being replaced by Al atoms (which must imply they leave vacancies in their wake), and that the created surplus leads to vacancy agglomeration [16].

Cu is a common trace element in Al-Mg-Si alloys, often as a residual from recycling, but it is also added on purpose by industry because it improves the material strength. In amounts as low as 0.1 wt % Cu can cause inter-granular corrosion [17]. Therefore, in this study the level has been kept at 0.05 wt %. When it comes to precipitate phases, Cu can substitute Al and Si sites within the structures but will also occupy sites at the precipitate interfaces [26-27]. Above some threshold Cu will suppress formation of β'' , promoting other phases to form. The precipitation sequence in Cu added 6xxx alloys can be given as follows [18] [19] [20] [21] [22].

Supersaturated solid solution \rightarrow atomic clusters \rightarrow Guinier-Preston-zones (pre- β'') [2] [3] \rightarrow β'' [6], L, S, C, QP, QC \rightarrow β' , Q' \rightarrow Q

In this work, for a 6060 alloy we remove a fraction of the solutes, Mg and Si, and replace it either fully (Mg atom for Li atom) or with a lower fraction of Cu or Li, alone or combined. We investigate the hardening response of the alloys as function of artificial ageing and compare with the reference alloys (the 6060 alloy and its leaner version). From TEM images and EELS thickness measurements, we obtain size and density statistics about the hardening precipitates in $\langle 001 \rangle_{\text{Al}}$ orientations when the alloys are at, or just prior to peak hardness conditions. Also, cross-sections from precipitates aligned in the viewing direction of the same conditions are investigated in more detail using high angle annular dark-field scanning TEM (HAADF-STEM), which is less affected by objective lens defocus and specimen thickness as compared to conventional HRTEM, hence consistently producing images of bright atomic columns

against a dark background [23] [24]. Finally, density functional theory (DFT) is applied to investigate how the formation enthalpy changes when Li incorporates into β'' , in the purpose of understanding important structural observations.

Experimental

Composition measurements (see Table 1) of the alloys were performed by inductively coupled plasma atomic emission spectroscopy.

The alloys were in the shape of cylindrical cast billets weighing 4 kg. They were homogenized for 3 hours within 1-2 hours prior to extrusion, performed at a temperature of 575 °C followed by air-cooling to room temperature (RT). The billets were heated to about 540 °C before extrusion into solid cylinders of 2cm diameter.

Cylindrical samples in lengths of 1 cm, cut perpendicular to the extrusion direction were heat treated according to the illustration in Fig. 1. Each sample was solution heat treated (SHT) at 535 °C in an air circulating furnace for 5 minutes, where after it was quenched in water to RT immediately after removal from the furnace. Furthermore, the samples were naturally aged for 4 hours at RT before being artificially aged (AA) at 195 °C.

Table 1 Alloy composition, effective solute (S_{eff}) and solute reduction ΔS relative to RX0

Alloy	Si ^a	Mg	Cu	Li	Fe	Mn	S_{eff} ^b	ΔS^c (- %)
RX0 wt%	0.45	0.37	–	–	0.20	0.03	0.77	–
RX0 at%	0.43	0.41	–	–	0.10	0.015	0.80	–
RX1 wt%	0.37	0.32	–	–	0.20	0.03	0.64	16.8
RX1 at%	0.36	0.36	–	–	0.10	0.015	0.66	16.7
RXL0 wt%	0.440	0.290	–	0.026	0.20	0.030	0.71	9.1
RXL0 at%	0.423	0.322	–	0.101	0.097	0.015	0.80	0.0
RXLC1 wt %	0.370	0.320	0.050	0.006	0.200	0.030	0.70	9.1
RXLC1 at %	0.356	0.356	0.021	0.023	0.097	0.015	0.71	11.3
RXL1 wt %	0.420	0.270	–	0.013	0.200	0.030	0.65	15.6
RXL1 at %	0.404	0.300	–	0.051	0.097	0.015	0.71	11.3

^a Effective Si available for precipitation (Si^*) is 0.05 wt % less the tabulated amount [25]. ^b Effective solute $S_{\text{eff}} = Mg + Si^* + Cu + Li$. ^c Removed solute fraction as percentage of content in RX0 (AA6060 reference alloy). RX1 is the leaner reference. 'L' and 'C' signify Li and Cu, respectively.

Details of heat treatments and TEM sample preparation are described in [12], TEM specimens were made from samples subjected to AA for 4 hours (close to peak hardness). Thin slices cut perpendicular to the extrusion direction were mechanically polished using SiC paper, to a thickness of approximately 100 μm . Disks of 3 mm diameter were stamped out from the foils and electrochemically thinned by a twin-jet Tenu-Pol 5 from Struers. The electrolyte consisted of 1 part nitric acid and two parts methanol, which was kept at approximately -25 °C by adding liquid nitrogen.

Behind the statistics of the precipitate microstructure presented in Table 2 are particle counts together with length and cross-section measurements extracted from TEM images, for this purpose acquired in a Philips CM30 instrument operated at 150 kV. The average thickness for each imaged area was estimated using parallel electron energy loss spectroscopy (PEELS). For a more complete description of the procedure leading to the statistics in Table 2, see [26]. In Table 2, the number densities and needle lengths are based on at least 1000 needles distributed over 8 – 10 imaged areas. The needle cross sections are averages from a minimum of 100 cross sections. The volume fractions are within 95 % confidence intervals. Although statistics generally originates from (the centre of) one grain from each alloy only, we inspected multiple grains to ensure that the microstructure was representative. For alloy RXL0, the images indicated strong local variations with a significant spread in needle sizes and number densities. Therefore, results in Table 2 from RXL0 are averages obtained from three different grains from three separate TEM specimens.

The HAADF-STEM images were acquired in a double corrected JEOL ARM200F, with 0.08 nm probe size and an inner HAADF collection angle of 50 mrad. Single images were acquired at 200 kV. Movies consisting of approximately 40 images were taken at 80 kV to correct drift and distortions by use of the Smart Align software [27]. Since ‘Smart Align’ uses a stack of images to do simple image translation, affine corrections and non-linear distortion corrections, these resulting images are much closer to the “real” imaged lattice with respect to atomic positions than corresponding single scans, and have a much higher signal-to-noise ratio. A stack of about 40 scans was used to create each ‘Smart Align’ image. A collection angle of 35 mrad was used for the ‘Smart Align’ images.

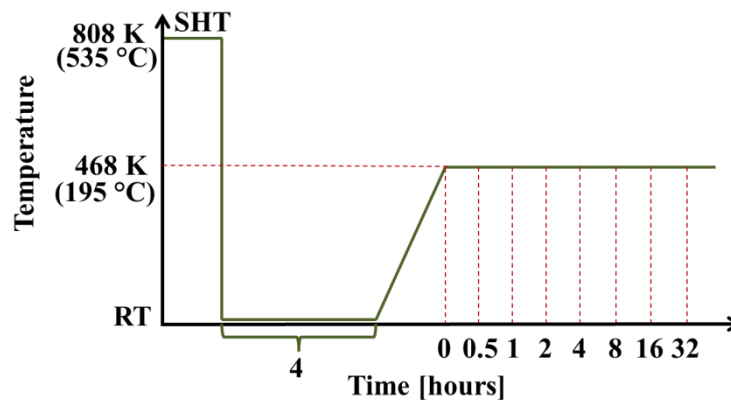


Fig. 1 Heat treatment overview. After quenching from solution temperature (535 °C), samples were held at RT for four hours before heated to the 195 °C artificial ageing temperature (at a rate 26 °C/hour). Vertical dotted lines indicate ageing times where water-quenching to RT completed the ageing.

For DFT calculations we used the Vienna ab initio simulation package (VASP) [28] [29]. The projector augmented wave method (PAW) within the PBE generalized gradient approximation was applied, with a plane wave energy cut-off of 400 eV. Gamma-centred k -points with maximal k -point distances of 0.25 \AA^{-1} in each direction were used for all the calculations. Methfessel-Paxton of 1st order was applied to relax the atomic positions to a maximum force

of 0.001 eV/Å. For accurate energies, a separate calculation was performed based on the tetrahedron method with Blöchl correction for smearing, which is explained in detail by Ninive et al. in [30].

3 Results

3.1 Vickers hardness, TEM and precipitate statistics

Fig. 2 is a plot of the age-hardening response of all alloys including the two references, where Vickers hardness (HV) is presented as a function of ageing time. The HV curves of RX0 (dense reference; originally used in industry) and RX1 (lean reference; reduced solute, but no additions) originate from an earlier study [12], but are presented here for comparison. The lean reference (RX1) ranges worst, the curve is well below all other alloys. RXL0 is a variation of RX0 with a quarter of Mg atoms substituted by Li, therefore containing the same amount of solute in atomic concentration. Table 2 shows the solute weighs 9.1 % less. The lithium addition in RXL0 compensates for the strength loss of the lean reference, reaching nearly identical peak hardness as the dense reference RX0, and even surpassing it for longer ageing times. The two other lithium added alloys, RXL1 and RXLC1, with slightly more solute than the lean reference, lay well above its curve. They show intermediate hardness values during the entire artificial ageing heat treatment. For longer ageing times RXLC1 is the more stable of the two alloys.

The four TEM micrographs given in Fig. 3 show typical morphology and distribution of the precipitates in the alloys. For RXL0, while the precipitate distribution generally is similar in all observable grains in the same specimens, in one specimen [Fig. 3 (a)] the precipitates were much coarser [compare with Fig. 3(b)]. As exemplified by the horizontal needle above the scale annotation in Fig. 3(a), a high amount of the coarser precipitates in RXL0 had wavy contrast lines in this specimen.

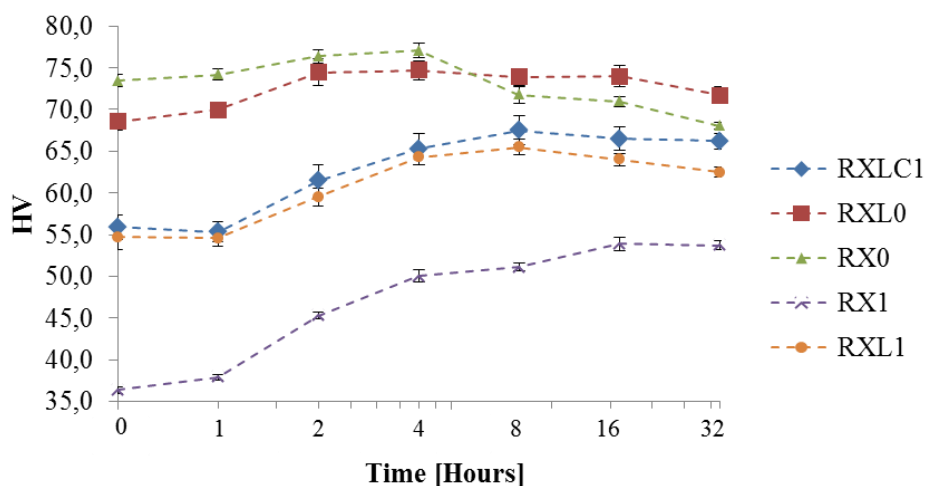


Fig. 2 Vickers hardness plotted as a function of artificial ageing time at 195 °C. Note that the x-axis has a logarithmic scale. RX0 (top) and RX1 (bottom) signify the dense and lean

reference alloys, respectively. Letters 'L' and 'C' indicate lithium and/or copper in an alloy (see Table 1).

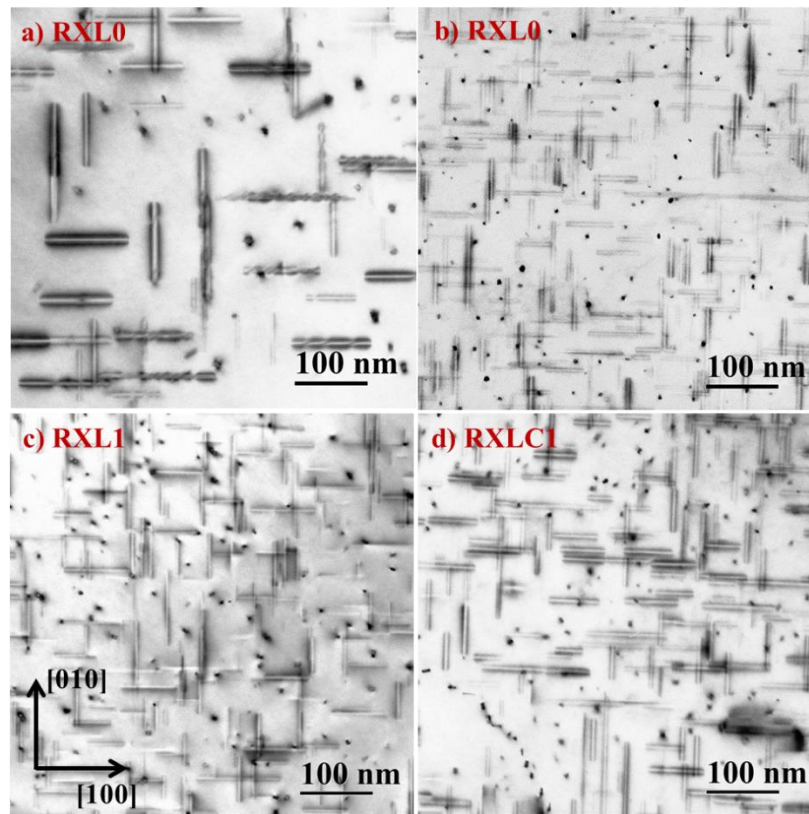


Fig. 3 TEM bright field images from each of the three Li-containing alloys at near peak hardness condition (4h AA at 195 °C). (a) RXL0, TEM specimen 1, (b) RXL0, TEM specimen 2 (c) RXL1 and (d) RXLC1. All images are taken along the $\langle 001 \rangle_{Al}$ zone axis. The double contrast lines in the micrographs are needles along the two $[100]_{Al}$ directions in the viewing plane. The crystal directions are indicated by arrows in (c).

Intriguingly, Table 2 shows that the high hardness for alloy RXL0 corresponds to lowest precipitate number density and volume fraction. The precipitates in this alloy are largest, being on average longest and with highest cross-section area.

Table 2 Precipitate statistics obtained after 4h AA at 195 °C. Average precipitate cross sections, needle lengths, number densities and volume fractions with corresponding errors estimated from TEM micrographs. RX0 and RX1 are included for comparison [12].

Alloy	Cross Section [nm ²]	Needle Length [nm]	Number Density [#/ μm^3]	Volume Fraction [%]	HV
RX0	24,0 ± 2,0	95 ± 5	3200 ± 400	{0.64, 0.80}	77
RXL0	17,5 ± 1,0	78 ± 3	3400 ± 400	{0.36, 0.43}	75
RXLC1	16,9 ± 1,6	61 ± 5	6100 ± 700	{0.54, 0,71}	65
RXL1	13,1 ± 0,7	56 ± 3	8000 ± 950	{0.53, 0.64}	65

3.2 HAADF-STEM and DFT

Fig. 4 shows HAADF-STEM images recorded in $\langle 100 \rangle_{Al}$ orientations showing cross-sections of precipitates representative of the various alloys near the hardness maximum. The observed cross-sections showed nearly just β'' structure, which means β'' is the foremost hardening phase in all alloys.

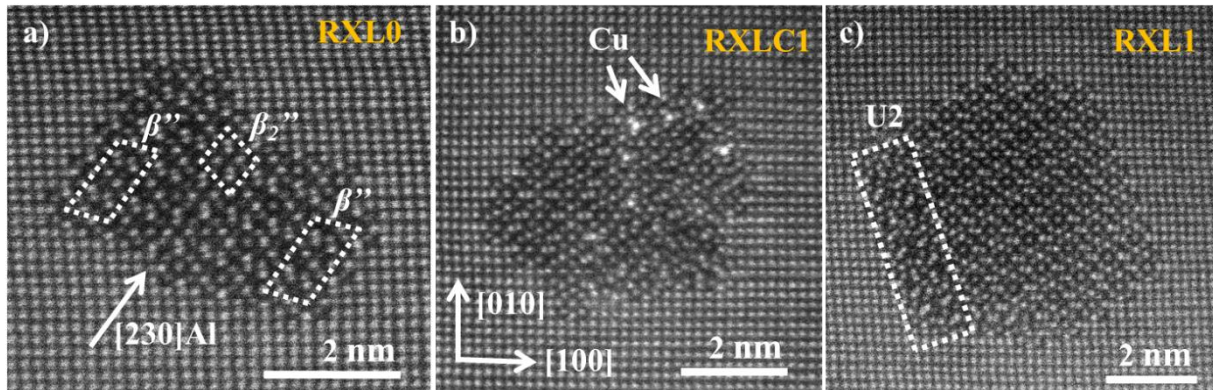


Fig. 4 Unprocessed HAADF-STEM images from (a) RXL0, the arrow points out a stacking fault along $a_{\beta''} \parallel \langle 230 \rangle_{Al}$. The dashed lines indicate β'' and β_2'' unit cells, (b) RXLC1, where bright Cu columns can be observed. Two Cu columns are pointed out by arrows. (c) RXL1, the dashed lines indicate a U2 region. The crystal directions, as indicated by arrows in (b), are the same in all three images.

Among features frequently observed in precipitate cross-sections of RXL0, was a stacking fault running across the width, along the direction $a_{\beta''} \parallel \langle 230 \rangle_{Al}$. Fig. 4 (a) shows one example. This stacking fault generates units of β_2'' across the cross section. In general, a high occurrence of β_2'' has been found in the Li-containing alloys. Based on the results presented in this section, models of the β'' -eyes are given in Fig. 5, with symbolic representation of elements given in Table 2. A significant amount of the Mg3 sites had a comparatively lower intensity than Mg1 and Mg2 sites in the HAADF-STEM images. Except for the Cu-containing alloy RXLC1, Fig. 4(b), not many precipitates were disordered, and other phases than β'' were practically non-present, although interfaces of β'' often could contain small regions of the U2 structure, see left side of the precipitate in Fig. 4 (c).

In RXLC1, a common triangular column group symmetry associated with Cu columns existed in several precipitate cross sections, exhibiting a high intensity in the HAADF-STEM images. Most cross sections contained a combination of fragments from both β'' and Cu-containing phases like Q' , C-plate and β'_{Cu} [17]. Several precipitate cross sections contained only a few Cu columns, with the remainder being β'' . Among the observed cross sections, those significantly smaller than the average presented in Table 2 incorporated no Cu columns at all.

Three representative examples from the ‘Smart Align’ images are presented in Figs. 5 and 6, with atomic overlays. The original β'' eye is shown in Fig. 5 (c) while the new model for Li-containing alloys is given in Fig. 5 (d). The symbolic representation of elements in Figs. 5 and 6 can be found in Table 3.

Table 3 Symbolic representation of elements in Figs. 5 and 6.

Elements / Height	Al	Si	Mg	Li
$z = 0.000$ nm	○	○	○	○
$z = 0.203$ nm	●	●	●	●

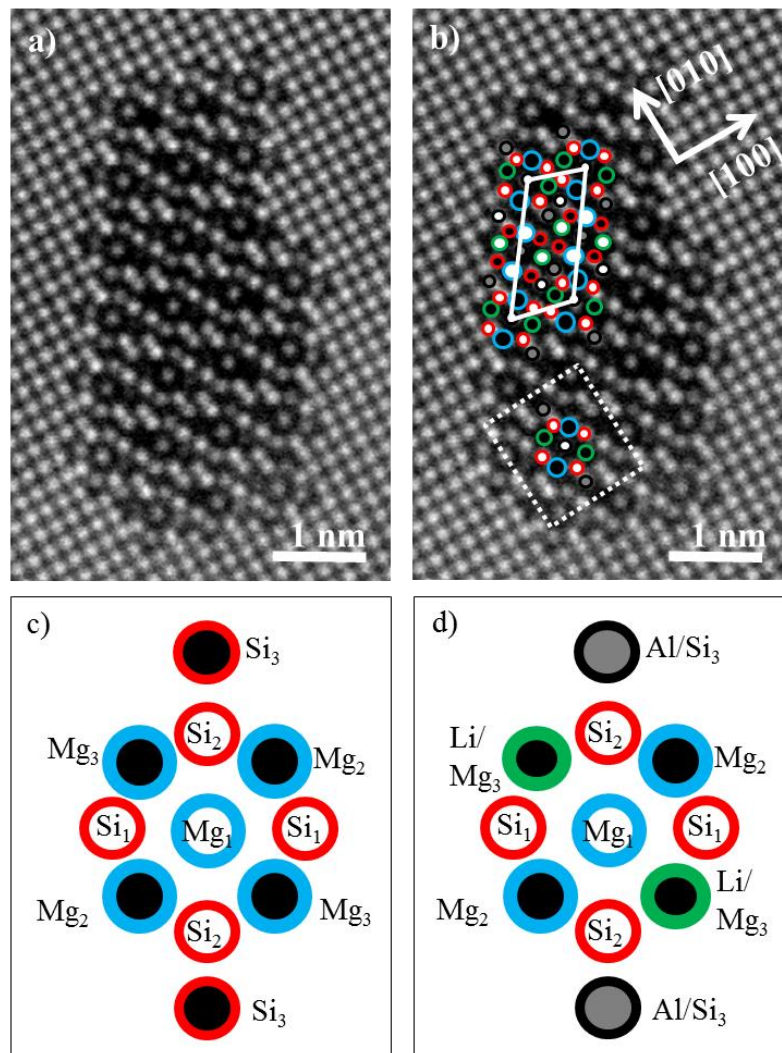


Fig. 5 (a) ‘Smart Aligned’ image of a β'' precipitate cross section in RXL0. (b) Partial atomic overlay on the precipitate in (a), where a unit cell of β'' is indicated by a white, solid line parallelogram and a single β'' -eye is indicated inside the white, dashed square. (c) The β'' -

eye as described in previous studies [30], (d) β'' – eye containing Li at Mg3 sites, directly comparable to the eyes of same heights in the β'' – unit cell. The elemental composition of the eye is based on intensity variations in HAADF-STEM ‘Smart Aligned’ images and DFT simulations. See Table 2 for symbolic representation of elements and heights.

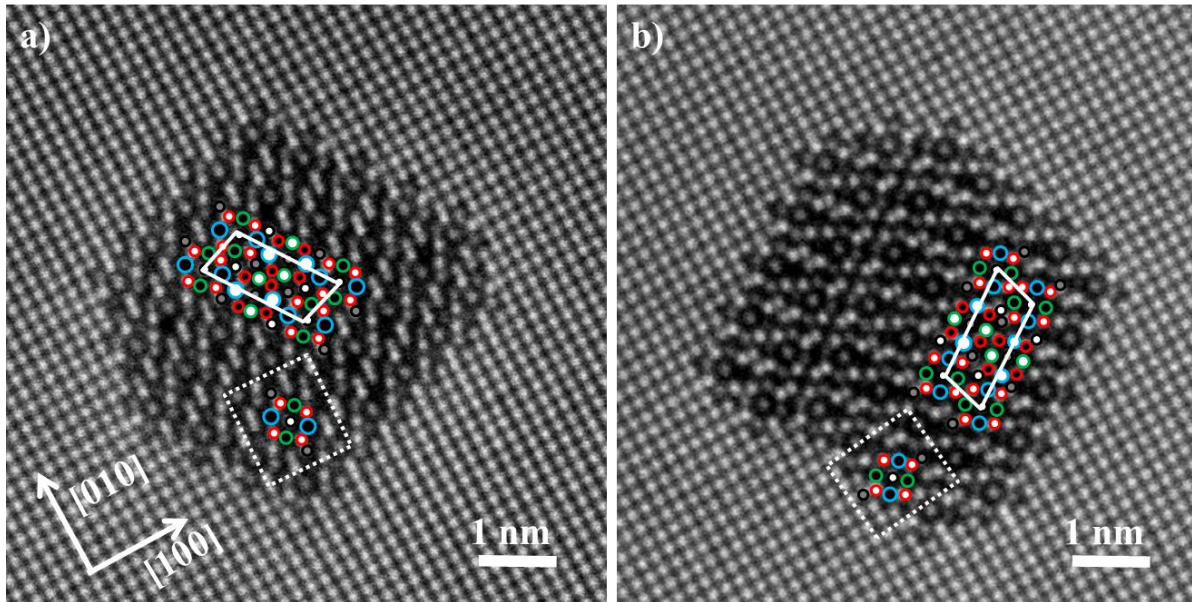


Fig. 6 ‘Smart Align’ HAADF-STEM images of two β'' precipitate cross section in RXL0, showing a different orientation of the unit cells, as compared to Fig. 5 (a), marked by solid white lines. Single β'' – eyes are also indicated inside the white dashed lines. Both orientations show less intensity at Mg3 sites, suggesting more Li occupancy. In (b) a stacking fault along $a_{\beta''} \parallel \langle 230 \rangle_{Al}$ is also present. See Table 2 for the symbolic representation of elements.

Based on the findings presented above, DFT calculations of the β'' (bulk) structure for various Li substitutions of the Mg sites was performed. The results are shown in Fig. 7. The curves show that a relatively high Li-occupancy at the Mg sites is energetically favourable. Substitution of Mg up to 60 % Li, i.e. to a formula $Mg_2Li_3Si_4Al_2$ seems to be the most favourable from Fig. 5, if the initial structure is $Mg_5Si_4Al_2$.

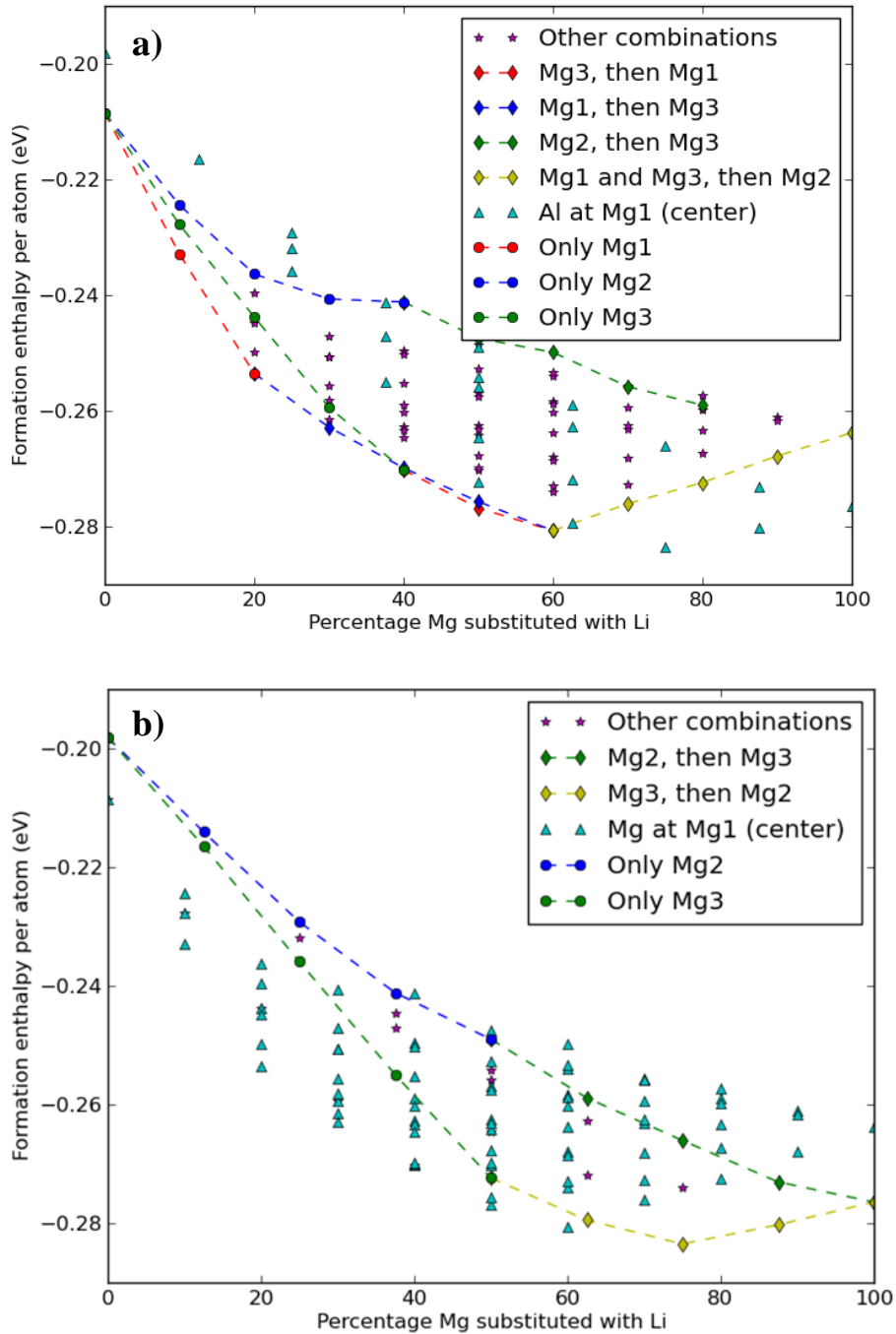


Fig. 7 DFT calculations showing the formation enthalpy per atom (eV) as a function of Li substituting Mg at different sites in the β'' eye. **(a)** Curves based on substitutions having $\text{Mg}_5\text{Si}_4\text{Al}_2$ as the initial structure (β'' with Al at Si3 sites). The blue pyramids correspond to the calculations presented in (b). **(b)** Curves based on substitutions having $\text{Mg}_4\text{Si}_4\text{Al}_3$ as the initial structure (β'' with Al at Mg1 and Si3 sites). The blue pyramids correspond to the calculations presented in (a). The formation enthalpy per atom is lowest for Mg at Mg1 sites up to about 60 % Mg substituted by Li.

4 Discussion

4.1 Hardness, TEM and statistics

RXL0 has the largest and most coarsely distributed precipitates of the three Li-added alloys, but also the highest hardness (see Table 2). According to previous investigations [12], the precipitate size correlating with maximum strength should fall between that of RXL0 and the two other alloys, RXL1 and RXLC1. One possible reason for this discrepancy is that RXL0 showed a large variation in the precipitate sizes and densities from one TEM specimen to another, indicating the acquired statistics is not sufficiently accurate for interpreting macroscopic properties. Such variation could arise if TEM specimens are taken from varying distances to the surface of the extruded rods. However, here it was taken care to avoid preparing TEM specimens close to the surface. A better explanation lies with the high diffusivity of Li: Li is a fast diffuser towards the surface of the material during heat treatments in air, which means depletion may reach far into the material [16] [31]. This would in turn lead to lower concentration of Li in some TEM specimens, causing an excess of Si for precipitation and more Si rich phases.

Another reason for the precipitate size and strength results could be a change in hardening mechanisms. Precipitates contribute to strength, since dislocations must pass them either by looping or cutting [32]. If the size distribution of the precipitate needles in RXL0 has reached a critical size, strength decreases both with larger and smaller precipitate needle sizes. A critical size will exist above which the strengthening mode changes to looping. Assuming similar interface energies for the precipitates in all three Li-added alloys (which is reasonable since the hardening phase is the same), we expect RXL0 to have a precipitate microstructure slightly larger than the critical size. Thus, such size should have a cross-section of about 15 nm^2 and a length of 70 nm, according to Table 2. However, according to previous studies the critical size of the related β' phase should be much larger [33], which suggests we need to investigate the above mentioned mechanisms further.

RXLC1 has better thermal stability than the similar, Cu-free, RXL1. Adding Cu to the alloy creates more disorder in the precipitate microstructure, which is evident for a majority of the observed precipitate cross sections in HAADF-STEM. The smaller precipitate cross sections, with respect to the size distribution, incorporate no Cu. The larger cross sections do however contain Cu columns. This could be due to precipitates containing Cu being more coherent, and has a higher probability of growing to larger sizes. Another possibility is that Cu diffuses more slowly than Si and Mg and does not take part in the precipitation and growth until after small needles of Si and Mg has already managed to form. For long ageing times, the reference alloy over-ages and becomes softer, while RXLC1 is comparatively more stable. As a consequence, the difference in strength between RXLC1 and the (stronger) dense reference RX0 becomes practically insignificant with time.

Earlier results have shown that alloys containing a combination of Ge and Cu in small amounts can have strong refining effects on precipitates [12]. The precipitate number densities in such

alloys reach much higher values than alloy RX0, and have higher accompanying hardness, as less coherent needles act as more effective dislocation impediments. If both strengthening modes are active, the precipitate distribution, size and type have a well-tuned balance for optimising material hardness. We plan further investigations to pinpoint the reason behind the local variations in the precipitate sizes and numbers, and the correlation between coarser precipitates and high hardness, for the Li substitution of Mg.

4.2 HAADF-STEM and DFT investigations

Close inspection of Mg columns in Figs. 5 and 6 shows that nearly all Mg3 sites not close to an interface have significantly lower intensity than Mg1 and Mg2 sites in the same eye. In Al-Mg-Si alloys with no other solute additions, intensity in HAADF-STEM changes much less between different sites [30]. Consequently, the differences here are likely to stem from Li occupation, predominantly in Mg3 columns.

From Fig. 7 we note that the lowest formation enthalpy configuration assuming an initial Mg₅Si₄Al₂ composition has 60 % Li substitution of the Mg sites, causing the Mg1 and Mg3 sites to fill up, while no substitution occurs at the Mg2 sites. Considering the low at % of Li added to the alloys, the Li occupancy is more likely to be below 20 % in Fig. 7. Filling Mg1 sites first and then Mg3 and vice versa does not seem to matter. Both sequences result in the same low formation enthalpy per atom. Mg1 sites have the largest “energetic gain” per atom and the Mg2 sites have the lowest gain per atom. However, Mg3 columns have twice as many atoms as Mg1 for each unit cell, which is one of the reasons why the Mg3 site gains more than Mg1 in Fig. 7.

From the experimental work, see Figs. 5 and 6, the low intensity at Mg3 sites appears systematic across the entire precipitate cross sections. However, less Li appear in Mg3 columns when the ‘eyes’ are adjacent to the Al-lattice or the commonly occurring stacking faults along $(230)_{Al}$. The same effects are observed for a majority of the β'' precipitate cross sections, suggesting that Li filling of Mg3 sites happens consistently for Li-added Al-Mg-Si alloys. One of the differences between Mg2 and Mg3 sites when considering the β'' structure is that the Mg2 sites have slightly more symmetric surroundings. Mg3 sites have less space in their near vicinity than Mg2 sites, which suggests it is more favourable to fill these sites with Li, as Li has a smaller atomic radius than Mg [34]. That is, the need to create a column taking up less volume might be higher at Mg3 sites.

The formation enthalpy per atom is significantly lowered when Mg1 sites are filled with Mg and not Al. It is possible that Li favours the “symmetric surroundings” at Mg1, because of the near-cubic symmetry with 12 nearest neighbours. The main conclusion is that it is most beneficial for Li to go to Mg3 and Mg1 sites first, while Mg2 sites are the last sites per eye to be replaced with Li. It is interesting that Mg1 sites are not exhibiting a darker contrast in HAADF-STEM considering the DFT results. We are planning quantitative STEM investigations to determine the Li occupation at different Mg sites in β'' .

5 Conclusions

The general objective in this work has been to investigate if strength in a 6060 alloy upon removal of a fraction of the solutes Si and Mg can be maintained, either by less heavy elements or by adding back lower amounts of other solute elements. Replacing about a quarter of the Mg solute with Li (0.1 at %) showed Li entering the main strengthening phase β'' without causing loss of strength. In fact, the alloy became slightly more temperature resistant. Replacement of a quarter of both Mg and Si with smaller and equal amounts of Li and Cu, whereby the weight fraction of solute was reduced by 9 % compared to its original value, resulted in a slight loss in strength. However, because of higher thermal stability, the strength loss approached zero after longer ageing times. Precipitate statistics acquired by conventional TEM enabled quantitative comparisons between the precipitate microstructures at peak hardness conditions. HAADF-STEM was used to study and compare the precipitate atomic structures. The alloy with 0.1 at % Li-replacement showed a microstructure comparable with the reference 6060 alloy. However, unexpected variations between TEM specimens were found, which are suspected to be linked to rapid Li depletion during heat treatment in air. HAADF-STEM showed that practically all the precipitate needles were of β'' type, with Li occupying a significant amount of the Mg₃ sites of the structure. This result was fully supported by density functional theory calculations.

Acknowledgements

The project has been supported through the BIA RolEx project, no. 219371 financed by Hydro Aluminium and the Research Council of Norway. The STEM work was carried out on the NORTEM JEOL ARM200F, TEM Gemini Centre, NTNU, Norway. The authors would also like to thank Birgitte Karlsen, SINTEF Materials and Chemistry for performing heat treatments and hardness measurements of the alloys.

Bibliography

- [1] C. D. Marioara, H. Nordmark, S. J. Andersen and R. Holmestad, *J. Mater. Sci.*, vol. 41, pp. 471 - 478, 2006.
- [2] G. A. Edwards, K. Stiller, G. L. Dunlop og M. J. Couper, *Acta Mater.*, vol. 46, pp. 3893 - 3904, 1998.
- [3] C. D. Marioara, S. J. Andersen, J. Jansen og H. W. Zandbergen, *Acta Mater.*, vol. 49, pp. 321 - 328, 2001.

- [4] S. J. Andersen, H. W. Zandbergen, J. Jansen, C. Træholt, U. Tundal og O. Reiso, *Acta Mater.*, vol. 46, pp. 3283 - 3298, 1998.
- [5] H. S. Hasting, A. G. Frøseth, S. J. Andersen, R. Vissers, J. C. Walmsley, C. D. Marioara, F. Danoix, W. Lefebvre og R. Holmestad, *J. Appl. Phys.*, vol. 106, 2009.
- [6] R. Vissers, M. A. v. Huis, J. Jansen og C. D. M. S. J. A. H. W. Zandbergen, *Acta Mater.*, vol. 55, pp. 3815 - 3823, 2007.
- [7] S. J. Andersen, C. D. Marioara, R. Vissers, A. Frøseth og H. W. Zandbergen, *Mater. Sci. Eng. A*, vol. 444, pp. 157 - 169, 2007.
- [8] S. J. Andersen, C. D. Marioara, A. Frøseth, R. Vissers og H. W. Zandbergen, *Mater. Sci. Eng. A*, vol. 390, pp. 127 - 138, 2005.
- [9] R. Vissers, C. D. Marioara, S. J. Andersen og R. Holmestad, *Aluminium Alloys*, vol. 2, pp. 1263 - 1269, 2008.
- [10] T. Saito, F. J. H. Ehlers, W. Lefebvre, D. Hernandez-Maldonado, R. Bjørge, C. D. Marioara, S. J. Andersen, E. A. Mørtzell og R. Holmestad, «Cu atoms suppress misfit dislocations at the β''/Al interface in Al–Mg–Si alloys,» *Scripta Materialia*, vol. 110, nr. 1, pp. 6-9, 2016.
- [11] E. A. Mørtzell, S. J. Andersen, J. Friis, C. D. Marioara og R. Holmestad, «Atomistic details of precipitates in lean Al-Mg-Si alloys with trace additions of Ag and Ge studied by HAADF-STEM and DFT,» *In progress*, 2016.
- [12] E. A. Mørtzell, C. D. Marioara, S. J. Andersen, J. Røyset, O. Reiso og R. Holmestad, «Effects of Germanium, Copper, and Silver Substitutions on Hardness and Microstructure in Lean Al-Mg-Si Alloys,» *Metallurgical and Materials Transactions A*, vol. 46, nr. 9, pp. 4369 - 4379, 2015.
- [13] I. Polmear, *Light Alloys, From Traditional Alloys to Nanocrystals*, Oxford UK1: Elsevier, 2006.
- [14] Y. Koshino, M. Kozuka, S. Hirosawa og Y. Aruga, «Comparative and complementary characterization of precipitate microstructures in Al-Mg-Si(-Li) alloys by transmission electron microscopy, energy dispersive X-ray spectroscopy and atom probe tomography,» *Journal of Alloys and Compounds*, vol. 622, pp. 765 - 770, 2015.
- [15] A. Sagara og K. Kamada, «Measurements of evaporation rate of Lithium from Al-Li alloy by depth profiling with an ion beam,» *Nuclear Instruments and Methods in Physics Research B*, vol. 44, pp. 373 - 376, 1990.

- [16] H. L. Jr og P. Coleman, «Vacancy clustering in quenched Al-Li solid solution alloys studied by Doppler broadening spectroscopy,» *J. Phys.: Condensed Matter*, vol. 10, pp. 10423 - 10428, 1998.
- [17] T. Saito, C. D. Marioara, S. J. Andersen, W. Lefebvre og R. Holmestad, «Aberration-corrected HAADF-STEM investigations of precipitate structures in Al-Mg-Si alloys with low Cu additions,» *Philosophical Magazine*, vol. 94, nr. 5, pp. 520 - 531, 2015.
- [18] C. D. Marioara, S. J. Andersen, T. N. Stene, H. Hasting, J. Walmsley, A. T. J. V. Helvoort og R. Holmestad, *Philosophical Magazine*, vol. 87, p. 3385, 2007.
- [19] D. J. Chakrabarti og D. E. Laughlin, *Prog. Mater. Sci.*, vol. 49, p. 389, 2004.
- [20] C. Cayron, L. Sagalowicz, O. Beffort og P. A. Buffat, *Philos. Mag. A*, vol. 79, p. 2833, 1999.
- [21] K. Matsuda, Y. Uetani, T. Sato og S. Ikeno, *Metall. Mater. Trans. A*, vol. 32, p. 1293, 2001.
- [22] L. Arnberg og B. Aurivillius, *Acta Chem Scand A*, vol. 34, p. 1, 1980.
- [23] T. Yamazaki, M. Kawasaki, K. Watanabe, I. Hashimoto og M. Shiojiri, *Ultramicroscopy*, vol. 92, p. 181, 2002.
- [24] P. D. Nellist og S. J. Pennycook, *Ultramicroscopy*, vol. 78, p. 111, 1999.
- [25] U. Tundal, O. Reiso, E. Hoff, R. Dickson og C. Devadas, i *Proc. 10th International Aluminum Extrusion Technology Seminar*, Miami, 2012.
- [26] C. D. Marioara, S. J. Andersen, H. W. Zandbergen og R. Holmestad, *Metall. Mat. Trans. A*, vol. 36, pp. 691 - 702, 2005.
- [27] L. Jones, H. Yang, T. J. Pennycook, M. S. J. Marshall, S. V. Aert, N. D. Browning, M. R. Castell og P. D. Nellist, «Smart Align - a new tool for robust non-rigid registration of scanning microscope data,» *Advanced Structural and Chemical Imaging*, vol. 1, 2015.
- [28] P. Hohenberg og W. Kohn, «Inhomogeneous Electron Gas,» *Phys. Rev.*, vol. 136, pp. B864 - B871, 1964.
- [29] K. W. og S. L. J., «Self-Consistent Equations Including Exchange and Correlation Effects,» *Phys. Rev.*, vol. 140, pp. A1133 - A1138, 1965.

- [30] P. H. Ninive, A. Strandlie, S. Gulbrandsen-Dahl, W. Lefebvre, C. D. Marioara, S. J. Andersen, J. Friis, R. Holmestad og O. M. Løvvik, «Detailed atomistic insight into the beta" phase in Al-Mg-Si alloys,» *Acta Materialia*, vol. 69, pp. 126 - 134, 2014.
- [31] T. Schmidt, S. Heun, J. Slezak, J. Diaz og K. C. Prince, «SPELEEM: Combining LEEM and Spectroscopic Imaging,» *Surface Review and Letters*, vol. 5, nr. 6, pp. 1287 - 1296, 1998.
- [32] J. D. Verhoeven, *Fundamentals of Physical Metallurgy*, London: John Wiley & Sons, 1975.
- [33] K. Teichmann, C. D. Marioara, S. J. Andersen og K. Marthinsen, «TEM study of β' precipitate interaction mechanisms with dislocations and β' interfaces with the aluminium matrix in Al-Mg-Si alloys,» *Materials Characterization*, vol. 75, pp. 1 - 7, 2013.
- [34] C. Wolverton, *Acta Mater.* , vol. 55, pp. 5867 - 5872, 2007.